

# Design of an UWB Indoor-Positioning System for UAV Navigation in GNSS-Denied Environments

Janis Tiemann, Florian Schweikowski and Christian Wietfeld  
TU Dortmund University, Communication Networks Institute (CNI)  
Otto-Hahn-Str. 6, 44227 Dortmund, Germany  
{janis.tiemann, florian.schweikowski and christian.wietfeld}@tu-dortmund.de

**Abstract**—Commonly used unmanned aerial vehicle (UAV) platforms rely on the use of global navigation satellite system (GNSS) receivers for navigation. To enable the autonomous navigation of cooperative UAVs in GNSS-denied environments, the use of an ultra-wideband (UWB) positioning system is proposed. This paper discusses the design and evaluation of a practical and cooperative UWB positioning system using newly available integrated radio frequency hardware and antennas. Constellation-aware parameters, as well as other effects like antenna characteristics, are taken into consideration. A non-line-of-sight rejection is implemented based on the ratio of the first path compared to the power of the cumulated channel impulse response. An experiment covering a range of positions and orientations is conducted to gain a broad, representative set of results to assess the system accuracy in real-life usage. In a first experiment the system performance achieves a root-mean-square error of under 10 cm in the horizontal plane and under 20 cm in the three-dimensional space with a probability of 95 %. A GNSS emulation system is implemented to evaluate the real-time in-flight use of the UWB positioning system on an experimental UAV carrier. A proof of concept is given that the GNSS emulation may be used with commercially available UAV platforms to augment those systems with indoor navigation capabilities.

**Keywords**—Ultra-wideband (UWB), Indoor-Positioning, Unmanned Aerial Vehicle (UAV), GNSS-Denied environments.

## I. INTRODUCTION AND RELATED WORK

Research and usage of cooperative unmanned aerial vehicles (UAV) systems [1] is often limited to outdoor experiments using traditional global navigation satellite system (GNSS) receivers for navigation. Vision-based control recently inspired extensive research in aerial robotics, allowing for complex and high-precision flight maneuvers [2]. However, those experiments were conducted using a complex and expensive motion capture system and off-board trajectory planning. A need for a low-cost, rapid deployment and decentralized indoor positioning system, enabling the indoor use of UAVs e.g. in emergency response scenarios [3], arose. Recent developments in ultra-wideband (UWB) communications offer high precision positioning through which a new range of applications is enabled [4]. The idea of ultra-wide bandwidth spread-spectrum impulse radio was discussed in [5] as a candidate for short-range communication. The ability to resolve multipath propagation makes it a viable candidate for indoor positioning, see [6]. Due to regulatory decisions and the definition of IEEE 802.15.4a [7], new complementary metal-oxide-semiconductor (CMOS) based UWB systems are seen as the basis of future wireless positioning systems, see [8]. Extensive research

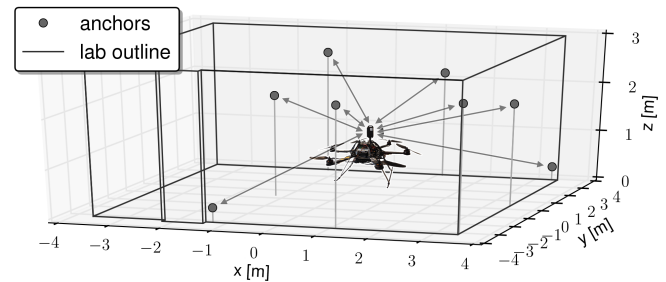


Fig. 1. Illustration of the UAV indoor-positioning scenario. The anchor positions represent the true positions used in the positioning experiments.

went into the theoretical limits of UWB ranging and positioning accuracy. Most of the experimental research was conducted using laboratory equipment, in time-difference-of-arrival (TDOA) setups ranging with single UWB pulses, see [9]. Although those experiments promise millimeter accuracy [10] of UWB positioning systems, their direct application is not practical in airborne systems due to the lack of integration, channel arbitration and clock synchronization. In this paper a practical positioning system implemented with low-cost and light-weight integrated UWB hardware is discussed. A study given in [11] used similar hardware. Static LOS scenarios were evaluated achieving a mean horizontal accuracy from 0.05 m to 0.4 m depending on the position and a mean positional accuracy ranging from 0.4 m to 1.0 m. In this work the system components influencing the positioning accuracy, will be independently assessed. An approach for basic non-line-of-sight (NLOS) rejection using a power comparison threshold will be evaluated. The positioning performance is improved to an horizontal accuracy of under 0.1 m in a complex dynamic scenario and a positional accuracy of under 0.2 m in 95 % of the measurements. A proof of concept GNSS emulation system will be introduced and developed to evaluate the performance of existing systems relying on GNSS for navigation.

## II. HARDWARE

The hardware node designed for this research, depicted in Fig. 2, is based on the newly available decaWave ScenSor DWM1000 module. The use of this module is beneficial in many aspects. A key aspect is that it could directly be integrated in custom circuits without an RF design. Alongside with the communication ability, the module allows a precise timestamping and a precise scheduling of messages. This makes it possible to implement either two-way-ranging (TWR) or TDOA based ranging and positioning applications. Due to

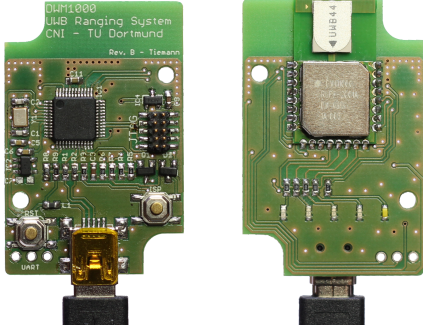


Fig. 2. UWB ranging nodes designed in the context of this work. Note the decaWave DWM1000 module mounted on the back of the node.

TABLE I. CHANNEL CONFIGURATION USED IN THE EXPERIMENTS.

$f_c$ [GHz]	$B$ [MHz]	$f_{pr}$ [MHz]	$R$ [kbps]	$c_{pr}$	$n_{pr}$
6.4896	499.2	64	850	9	256

the low level register based interface over SPI, all of the application logic (e.g. TWR) is handled by the host processor. This fine-grained control over each parameter in the communication allows for a flexible and versatile use of the system. Although the host controller software gets very complex, the fine-grained control is still beneficial for scientific applications, based on the fact that many diagnostics can be assessed and therefore a detailed control over the system is possible. Due to the low-cost ( $\sim 50$  \$), small-size (44 x 29 mm) and lightweight ( $\sim 5$  g) construction a versatile and rapid deployment in infrastructure as well as in mobile systems is possible.

### III. POSITIONING FACTORS

#### A. Ranging Performance

The ranging was conducted using symmetric-double-sided two-way-ranging (SDS-TWR) [12]. This ranging method eliminates the need for clock synchronization as opposed to TDOA based systems [13]. That makes the TWR based localization more precise, but comes with the downside of a higher channel usage since 3-4 messages are needed for each ranging executed in the system. The ranging performance is listed in Tab. II. Eight measurements with  $n$  samples at different distances  $d$  were conducted using the channel configuration with a carrier frequency  $f_c$ , a bandwidth  $B$ , a preamble frequency  $f_{pr}$ , a bit-rate  $R$ , the preamble code  $c_{pr}$  and the number of preamble symbols  $n_{pr}$  as listed in Tab. I. The mean error  $\mu_e$  is listed next to the root-mean-square error  $\mu_{|e|}$  and the standard deviation

TABLE II. RANGING STATISTICS

$d$ [m]	$\mu_e$ [m]	$\mu_{ e }$ [m]	$\sigma_e^2$ [m]	$\mu_{\phi_{fp}}$ [dB]	$\sigma_{\phi_{fp}}^2$ [dB]	$n$
0.6	0.003	0.014	0.016	-1.94	0.530	10091
1.2	-0.002	0.013	0.016	-1.80	0.321	10175
1.8	0.049	0.049	0.015	-2.84	0.208	10161
2.4	0.060	0.060	0.019	-2.73	0.291	12813
3.0	0.050	0.050	0.018	-2.83	0.290	10174
3.6	0.043	0.044	0.022	-3.55	0.260	11552
4.2	0.041	0.041	0.018	-3.56	0.416	10372
4.8	0.033	0.034	0.022	-2.87	0.305	13891

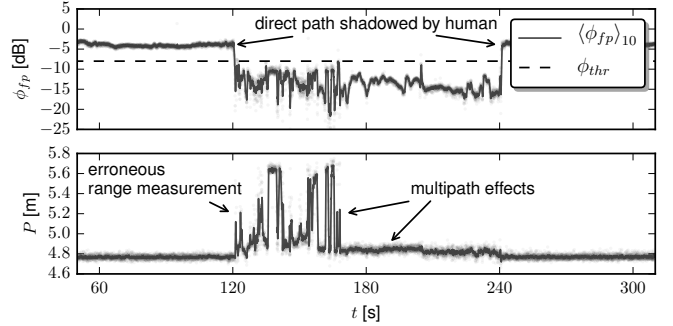


Fig. 3. Results of an NLOS experiment at  $d = 4.8$  m. Note the strong variance of the pseudorange  $P$  in the first part of the shadowing.

of the error  $\sigma_e^2$ , where a positional error of  $\pm 1$  cm has to be taken into consideration.

#### B. NLOS Detection

The modules provide a way to access the channel impulse response (CIR) of the received signals as a correlation of the received preamble symbol with the reference pulse, see [14]. This allows for first path detection and therefore precise time-of-arrival (TOA) reconstruction. The power of the first path is reconstructed using the first three parts of the CIR register. The estimation of the accumulated power of the CIR is  $P_{cir}$ . A new metric, the first path ratio  $\phi_{fp}$ , is used to distinguish between line-of-sight (LOS) and NLOS. This ratio is calculated as the difference of  $P_{fp}$  and  $P_{cir}$ , see (1). Since  $P_{fp}$  and  $P_{cir}$  are calculated as logarithmic values, the difference in logarithmic scale shows the ratio of both powers.

$$\phi_{fp}[\text{dB}] = P_{fp}[\text{dBm}] - P_{cir}[\text{dBm}] \quad (1)$$

Due to the fact that a reflected signal holds less power and is more ambiguous than a signal received from the direct path, because of multiple interfering reflections, the first path ratio gives an indicator for possible NLOS conditions. The case-decision for NLOS detection based on the threshold  $\phi_{thr}$  is shown by (2).

$$RX = \begin{cases} LOS & \text{for } \phi_{fp} > \phi_{thr} \\ NLOS & \text{for } \phi_{fp} \leq \phi_{thr} \end{cases} \quad (2)$$

To validate the assumption, that NLOS conditions can be detected by the system based on the first path ratio  $\phi_{fp}$  the following experiment was conducted. A tag and an anchor were placed at  $d = 4.8$  m distance in LOS condition. After  $t = 120$  s a human is shadowing the direct path. As shown by Fig. 3, this shadowing is detectable by assessing  $\phi_{fp}$ . The transition is immediate and always under the threshold  $\phi_{thr} = -8$  dB. The pseudorange  $P$  is influenced directly by this shadowing as an error is introduced to the range measurement. A strong variation of  $P$  is noticeable in  $120 \text{ s} < t < 170 \text{ s}$ . It is assumed that this variation results due to a strong indirect path close to the tag caused by a metal desk leg. This strong indirect path is also indicated by a high variation of  $\phi_{fp}$  in this timeframe. A NLOS rejection threshold of  $\phi_{thr} = -10$  dB was used in the following experiments.

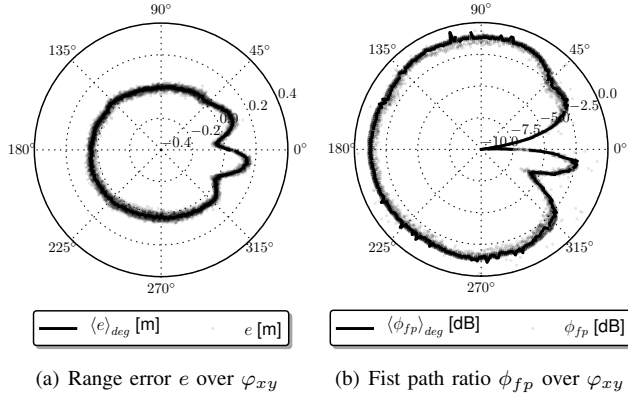


Fig. 4. Experimentally measured antenna characteristics of the node at  $f_c = 6.5$  GHz. A discrete average filtering over each degree yields the filtered range error  $\langle e \rangle_{deg}$  and the filtered first path ratio  $\langle \phi_{fp} \rangle_{deg}$ .

### C. Antenna Characteristics

The impact of the antenna characteristics on the ranging performance is analyzed in the following experiment. While one anchor resides at a static position, the tag is rotated. This rotation is conducted using a rotary mount allowing for precise angular control. This procedure allows a reconstruction of the angle dependent ranging error  $e = P - \langle P \rangle$ . The angle dependent antenna group-delay  $\tau_g = e/c$  corresponds directly to the speed of light  $c$ . Due to the discrete steps of  $\varphi$ , the results are averaged per degree, denoted in  $\langle e \rangle_{deg}$  and  $\langle \phi_{fp} \rangle_{deg}$ . Note that the antenna characteristics are highly dependent on the carrier-frequency  $f_c$ . The channel configuration used in this experiment is listed in table I. The characteristic of main interest for most applications is the rotation around  $\varphi_{xy}$  as illustrated in Fig. 4(a). An uniform distribution of  $e$  can be seen from an angle  $45^\circ < \varphi_{xy} < 315^\circ$ . The distribution of the first path ratio  $\phi_{fp}$  shown in Fig. 4(b), confirmed the non uniform distribution of  $e$  as  $\phi_{fp}$  indicates a pole at  $\varphi_{xy} = 0^\circ$ . It is shown that the orientation of the antenna has significant impact on the rangings.

### D. Constellation Quality

The accuracy of the position determination is dependent on the constellation of the anchors and the position of the tag itself, see [15]. The quality parameter is called dilution of precision (DOP). A lower DOP yields a better positioning capability. To asses the quality of a constellation, the horizontal

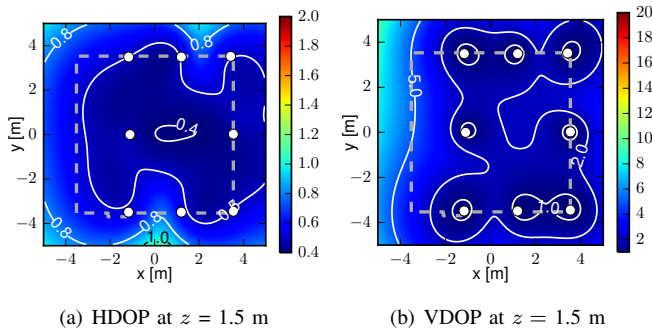


Fig. 5. Calculated heatmap of the DOP representing the distribution of the positioning capability at different points in the laboratory setup from above.

DOP (HDOP) and the vertical DOP (VDOP) of a tag was evaluated over each position at height  $z = 1.5$  m of the laboratory setup shown in Fig. 5. Because of the practical constraints of anchor positioning and application requirements, the anchor constellation was chosen in favor of precise horizontal positioning. Therefore the HDOP is much smaller than the VDOP depicted in Fig. 5.

## IV. EXPERIMENTAL EVALUATION OF THE POSITIONING SYSTEM ACCURACY

### A. Positioning Method

The analyzed cooperative indoor positioning system consists of nine UWB nodes. Eight nodes are configured to act as anchors, listening for ranging requests as depicted in Fig. 1. One node though is configured as a tag, ranging with a fixed set of anchors in a round-robin schedule. The obtained pseudorange  $P^k$  of the measurement  $k$  is the addition of the geometrical distance  $\rho^k$  and the error introduced by the measurement  $e^k$ , see (3).

$$P^k = \rho^k + e^k \quad (3)$$

To find a solution for the equation system, that minimizes  $e^k$  for all measurements  $k$ , a least squares approach is used. Because of the non-linearity introduced by  $\rho^k = \sqrt{(x - x_k)^2 + (y - y_k)^2 + (z - z_k)^2}$ , the system needs to be linearized. This is done using an iterative procedure that successively approximates the values of the receiver position. A first-order Taylor series expansion is used to calculate the increments on the receiver position. Each iteration step  $i$  updates the estimation of  $x_i$ , see (4). If no estimation for the initial position at  $i = 0$  is available, the center of the coordinate system  $x_0 = (0, 0, 0)^T$  is chosen. This procedure is a special form of the commonly known Gauss-Newton algorithm used to solve non-linear least squares problems [16].

$$\min_{x_i} \|A_i x_i - b_i\|_2 \quad (4)$$

### B. Dynamic Tracking Capabilities

To qualitatively asses the system capabilities in a practical use-case, an experiment of tracking a person holding a tag was conducted. The person is moving along the tile pattern of the floor in the laboratory. This meander movement is covering the whole walkable area of interest. Since the person does not move in a defined way, quantitative error assessment is not possible in this case. However, a qualitative evaluation of the results is still possible.

The results of the tracking experiment are depicted in Fig. 6. The raw positioning results are filtered with a Kalman filter, illustrated are the state estimates  $\langle H \rangle_K$ . A moving window filter  $\langle H \rangle_{10}$  is also applied. The movement is identifiable and the meander pattern is clearly reconstructable. However, the lines along the y axis at the transitions of the meander are not perfectly aligned, this is due to the uncontrolled nature of the movement, where the person itself is introducing a variation while changing directions. Therefore only the lines along the x axis of the meander clearly follow the reference movement  $H_r$ . It is shown that the system is capable of

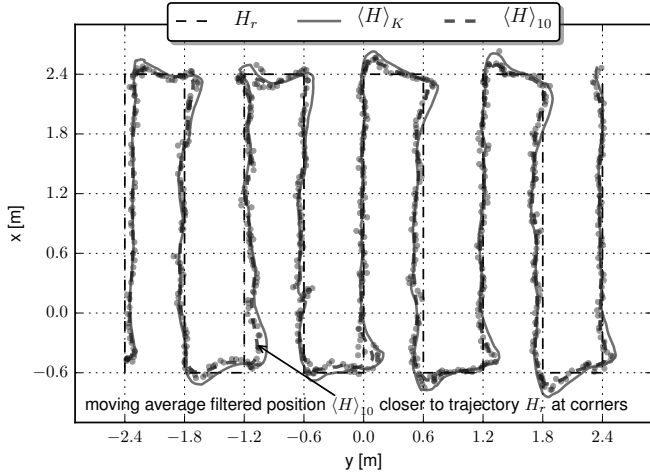


Fig. 6. Horizontal positioning results of a dynamic tracking experiment. A person walking along a meander trajectory  $H_r$ , holding a tag is tracked. Note the difference between the moving window filtered trajectory  $\langle H \rangle_{10}$  and the Kalman estimate  $\langle H \rangle_K$ .

tracking dynamic movement, such as the movement of a person. The positioning results do not show a strong qualitative variation of the positioning capability over the area of interest. It should also be noted that multiple orientations of the tag were considered, as the person changed the walking direction. Although the Kalman filter produces an overshoot, depicted in Fig. 6, in the used configuration it works best for objects underlying a low acceleration. Since the person tried to walk along a meander trajectory, abrupt direction changes have to be considered, causing the overshoot of the Kalman estimate  $\langle H \rangle_K$ .

### C. Quantification of System Capabilities

As seen in section III-C, the antenna directivity is influencing rangings and therefore positioning results. Hence, the position of the tag itself is not the only parameter that has to be taken into account. To achieve meaningful results in positioning, the assessment is narrowed down to a typical use-case. Precise horizontal positioning with a fixed  $z$  axis orientation is considered as the main application for the system. In order to evaluate the error of a moving tag, a controlled movement has to be performed. To produce a controlled movement, the tag was mounted to an arm, fixed on a rotation mount. The mount is then rotated around  $360^\circ$  with a low acceleration and velocity to reduce flexing of the arm. Note that the arm is speed-controlled, so the angle can be reconstructed from the recording time. Since the tag is mounted directly to the arm, it changes orientation with the angle of rotation  $\varphi$ . This procedure allows not only a qualitative assessment of the positioning results, but also a quantitative evaluation, since the actual position of the tag is known in any point of time.

To quantify the overall absolute errors defining the positioning capabilities of the system, the cumulative distribution functions of the errors are evaluated in Fig. 8. The error quantiles, listed in Tab. III quantify those results. Due to the anchor constellation, the horizontal positioning accuracy is expected to be better than the vertical one. This assumption is confirmed by the positioning results. With a probability of 95 %, the horizontal error is less than 10 cm. The overall

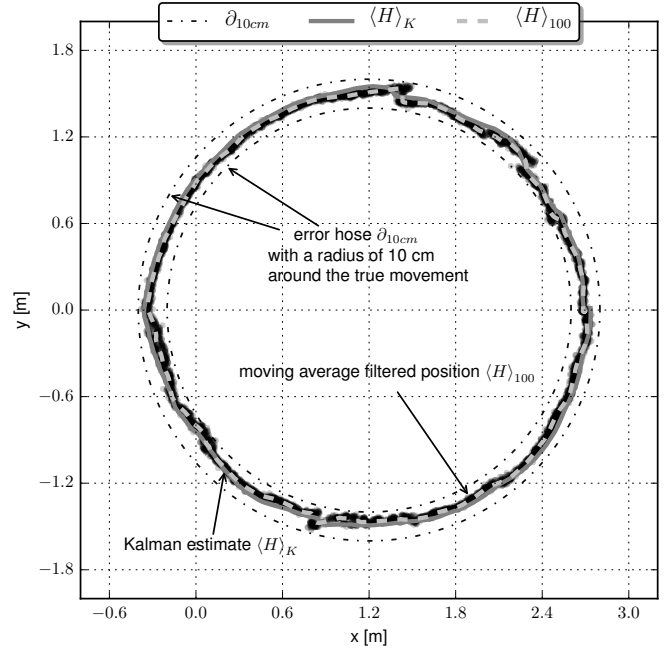


Fig. 7. Results of the controlled circular motion experiment in the horizontal plane. The unfiltered, moving window filtered positions  $\langle H \rangle_{100}$  and the Kalman filtered estimations  $\langle H \rangle_K$  are depicted. Note the error hose  $\delta_{10cm}$ .

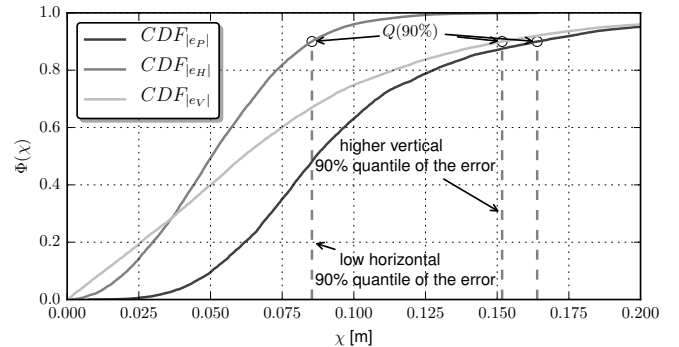


Fig. 8. Cumulative distribution functions of the absolute errors  $|e_P|$ ,  $|e_H|$  and  $|e_V|$ . The 90 % quantiles of the errors are shown. Note the difference between the horizontal and the vertical error distribution.

positioning performance can be quantified with an absolute positional error of under 20 cm in 95 % of all measured positions. Due to the complex experiment setup, covering a whole range of positions and orientations, this can be seen as a representative result.

TABLE III. ERROR QUANTILES FOR THE POSITIONAL SPACE P, THE HORIZONTAL PLANE H AND THE VERTICAL AXIS V.

	$Q(50\%)$ [m]	$Q(75\%)$ [m]	$Q(90\%)$ [m]	$Q(95\%)$ [m]	$Q(99\%)$ [m]	$n$
P	0.087	0.117	0.164	0.198	0.273	8960
H	0.050	0.069	0.085	0.096	0.121	8960
V	0.062	0.100	0.152	0.187	0.264	8960

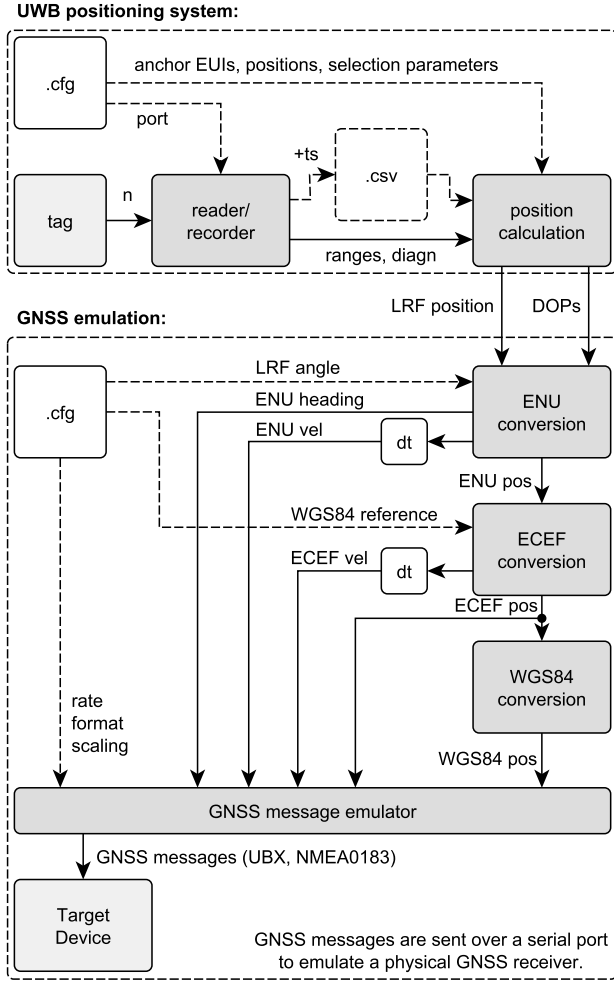


Fig. 9. Illustration of the system components of the UWB positioning system and the GNSS emulation. Note the modularity of the system, as the only interface is the current LRF position and DOP.

## V. GNSS EMULATION

One of the challenges in indoor-navigation is to work with already existing autonomous robotic systems. Many platforms are closed source and only a higher level interface is provided. Especially UAV systems rely on the use of GNSS receivers for navigation. In this paper, the emulation of commonly used GNSS receivers to ensure compatibility with a wide range of platforms is proposed. This comes with the benefit of already existing protocols and navigation controller implementations based on GNSS reception. However, commercially available platforms usually come as a black-box and, therefore, debugging is difficult. One of the steps necessary is the emulation of the receiver specific navigation messages including velocities in the cartesian coordinate systems for most control algorithms. A full set of navigation messages [17] has to be provided to ensure compatibility with a wide range of systems. This includes the calculation or estimation of all GNSS specific parameters provided by GNSS receivers as shown in Fig. 9.

Due to this, a set of coordinate systems has to be provided [18]. The definition of a local reference frame (LRF) is most practical for indoor use. The LRF is a cartesian coordinate

system formed from a plane tangent at a reference point on the earth's surface. An angle  $\rho$ , describing the rotation around the vertical axis at this point, is defining the orientation towards the east axis of the commonly used easting  $e$ , northing  $n$  and upping  $u$  (ENU) coordinates. A simple rotation converts LRF to ENU coordinates, see (5).

$$\begin{pmatrix} e \\ n \\ u \end{pmatrix} = \begin{pmatrix} \cos(\rho) \\ \sin(\rho) \\ 0 \end{pmatrix} x' + \begin{pmatrix} \sin(\rho) \\ \cos(\rho) \\ 0 \end{pmatrix} y' + \begin{pmatrix} 0 \\ 0 \\ 1 \end{pmatrix} z' \quad (5)$$

The transformation from local ENU to global cartesian Earth Centered Earth Fixed (ECEF) coordinates is possible without intermediate steps. The ECEF coordinates  $(x, y, z)^T$  can be calculated based on the reference position in geodetic coordinates  $(\lambda_r, \varphi_r, 0)$  as shown in (6).

$$\begin{pmatrix} x \\ y \\ z \end{pmatrix} = \begin{pmatrix} -\sin(\lambda_r) \\ \cos(\lambda_r) \\ 0 \end{pmatrix} e + \begin{pmatrix} -\cos(\lambda_r) \sin(\varphi_r) \\ -\sin(\lambda_r) \sin(\varphi_r) \\ \cos(\varphi_r) \end{pmatrix} n + \begin{pmatrix} \cos(\lambda_r) \cos(\varphi_r) \\ \sin(\lambda_r) \cos(\varphi_r) \\ \sin(\varphi_r) \end{pmatrix} u \quad (6)$$

To transform coordinates from ECEF coordinates to the World Geodetic System 1984 (WGS84) which is commonly used in GNSS applications, the prime vertical of curvature  $N$  has to be calculated from the semi-major equatorial axis  $A$  of the ellipsoid and the eccentricity  $E$ , both defined in the WGS84 model, see (7).

$$N = \frac{A}{\sqrt{1 - E^2 \sin^2 \varphi}} \quad (7)$$

The semi-major polar axis  $b$  of the ellipsoid has to be calculated along with the flattening  $e_p$ , the radius  $p$  and the auxiliary  $\theta$ , see (8), (9), (10) and (11).

$$b = \sqrt{A^2(1 - E^2)} \quad (8)$$

$$e_p = \sqrt{\frac{A^2 - b^2}{b^2}} \quad (9)$$

$$p = \sqrt{x^2 + y^2} \quad (10)$$

$$\theta = \arctan\left(\frac{Az}{bp}\right) \quad (11)$$

After those intermediate values are calculated, the latitude  $\lambda$ , longitude  $\varphi$  and height over the ellipsoid  $h$  can be deducted as shown in (12).

$$\begin{aligned} \lambda &= \arctan\left(\frac{y}{x}\right) \\ \varphi &= \arctan\left(\frac{z + E^2 b \sin^3(\theta)}{p - E^2 A \cos^3(\theta)}\right) \\ h &= \frac{p}{\cos(\varphi)} - N \end{aligned} \quad (12)$$

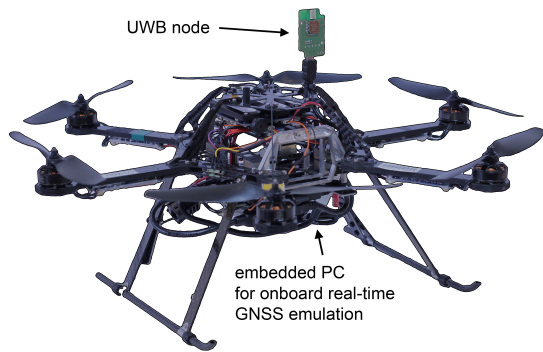


Fig. 10. UAV platform for proof of concept flight evaluation. UAV carrier based on an AscTec FireFly and equipped with the UWB node developed during this work.

## VI. EXPERIMENTAL PROOF OF CONCEPT

To evaluate the performance of the UWB positioning system detailed in section IV-A and the GNSS Emulation proposed in section V, a proof of concept experiment was conducted. An UWB node was mounted on an UAV carrier as depicted in Fig. 10. The node was connected to an embedded PC, running a standard linux based operating system. An application calculating the local positions from the UWB positioning system, transforming them into global coordinates, and providing them over a serial port in the form of standardized GNSS messages was used to feign a physical GNSS receiver to the UAV platform.

The UAV was flown manually in the center of the laboratory and switched over into a position-hold mode, where the system tries to keep the last known horizontal position  $H_{home}$  via the information gained through the compass and the GNSS receiver, as depicted in Fig. 12. Due to the insufficient horizontal accuracy of common GNSS systems, height-control is based on inertial and barometric measurements. The experiment carrier was held in position-hold for 220 s and then manually landed.

The Kalman filtered recorded trajectory  $\langle H_t \rangle_K$  of the flight in the context of the laboratory setup is depicted in Fig. 11. As clearly visible by  $Q(95\%)$ , the system autonomously achieves to hold its position in-flight with a radius  $r = 0.369$  m with a probability of 95 % of the unfiltered positioning results. A quantification of the horizontal position deviation in form of error quantiles  $Q(50\%)$  to  $Q(99\%)$  with  $n$  samples from the home position  $H_{home}$  is listed in in Tab. IV. The vertical and, therefore, positional deviation is not listed since the height is held with the barometric sensor, which is not part of this research. It should be noted that the trajectory is based on recordings made with the UWB positioning system, so the results have to be seen in the context of the accuracy achieved with the positioning system itself.

During the experiments it became obvious that navigation performance is tightly coupled with magnetometer perfor-

TABLE IV. ERROR QUANTILES FOR THE HORIZONTAL PLANE H.

	$Q(50\%)$ [m]	$Q(75\%)$ [m]	$Q(90\%)$ [m]	$Q(95\%)$ [m]	$Q(99\%)$ [m]	$n$
H	0.176	0.246	0.322	0.369	0.449	1000

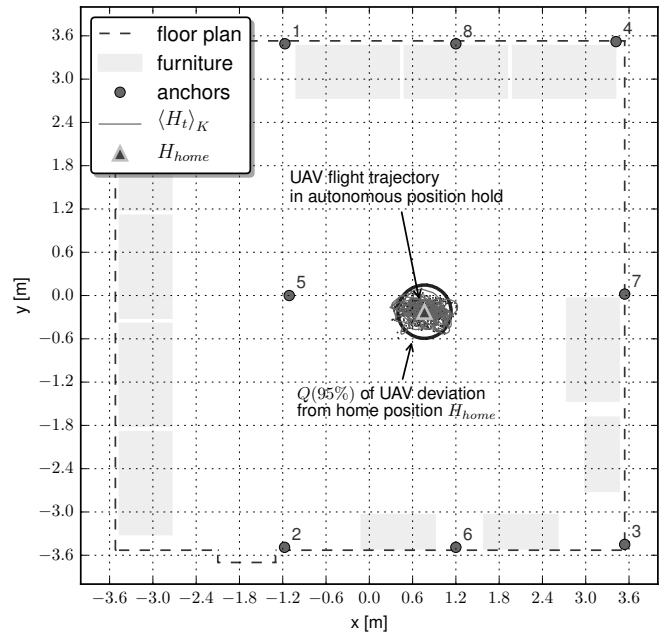


Fig. 11. Recorded trajectory of UAV in position hold in the laboratory setup. A flight with a duration of 220 s was conducted based on the real-time GNSS emulation provided by the UWB positioning system.

mance, as magnetometer readings are needed to calculate the position correction direction in navigation control algorithms. This leads to a non-optimal performance in environments with strong magnetic fields. In the context of the presented results, a variation of orientation along the yaw axis was observed leading to the assumption that magnetometer errors are responsible for the oscillation visible in Fig. 11. Other factors, directly influencing the navigation capabilities, were the calculated velocities and headings, as they seem to be used directly by the navigation controller. Therefore, reasonable filtering is required to remove strong peaks in the velocity values introduced by noise on the position itself.

## VII. CONCLUSION

In this paper, a cooperative positioning system for indoor UAV navigation utilizing highly integrated IEEE 802.15.4a

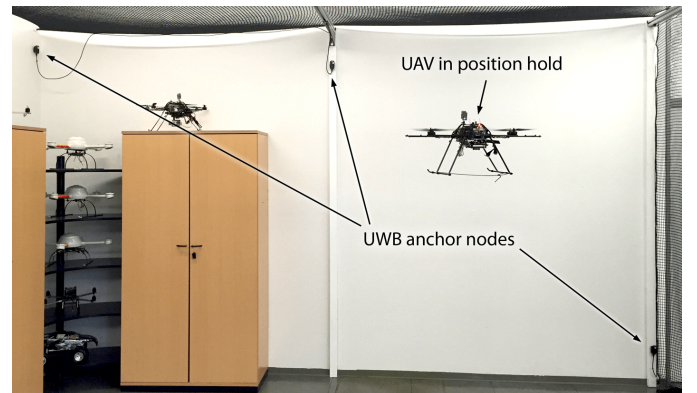


Fig. 12. Photo of UAV in the indoor proof of concept flight. The UAV platform is holding its position based on the inputs of the GNSS emulation. Note the small size of the anchor nodes mounted to the walls.

compliant RF hardware, was introduced. The effects of different system components on the positioning accuracy were highlighted. A 95 % probability positioning accuracy of 10 cm in the horizontal plane and 20 cm in the three-dimensional space was experimentally achieved enabling control level applications, like UAV indoor navigation. An on-board real-time GNSS emulation on an embedded system was introduced, providing position information in multiple coordinate systems. A method for refitting existing mobile autonomous robotic systems with indoor navigation capabilities was proposed using feigned GNSS messages. A proof of concept experiment showed a successful autonomous indoor position hold flight of a commercially available UAV platform, using the proposed method. The UAV was able to hold its position in a radius of under 50 cm. More research is required to optimize the filtering for the UAV specific navigation controller as well as resolving magnetometer issues indoors, maybe with the help of integrated measurement unit (IMU) sensor fusion, to achieve improved flight performance.

#### ACKNOWLEDGEMENT

The work on this paper has been partially funded by Deutsche Forschungsgemeinschaft (DFG) within the Collaborative Research Center SFB 876 “Providing Information by Resource-Constrained Analysis”, project A4, received funding from the European Union Seventh Framework Programme (FP7/2007-2013) under grant agreement 261769 and has received funding from the federal state of Northrhine-Westphalia and the “European Regional Development Fund” (EFRE) 2014-2020 in the course of the “CPS.HUB/NRW” project under grant number EFRE-0400008.

#### REFERENCES

- [1] N. Goddemeier, S. Rohde, and C. Wietfeld. Experimental validation of RSS driven UAV mobility behaviors in IEEE 802.11s networks. In *Globecom Workshops (GC Wkshps), 2012 IEEE*, pages 1550–1555, Dec 2012.
- [2] S. Lupashin, M. Hehn, M. W. Mueller, A. P. Schoellig, M. Sherback, and R. D’Andrea. A platform for aerial robotics research and demonstration: The flying machine arena. *Mechatronics*, 2014.
- [3] S.J. Ingram, D. Harmer, and M. Quinlan. Ultrawideband indoor positioning systems and their use in emergencies. In *Position Location and Navigation Symposium, 2004. PLANS 2004*, pages 706–715, Apr 2004.
- [4] M. Vossiek, L. Wiebking, P. Gulden, J. Weighardt, and C. Hoffmann. Wireless local positioning - concepts, solutions, applications. In *Radio and Wireless Conference, 2003. RAWCON '03. Proceedings*, pages 219–224, Aug 2003.
- [5] M.Z. Win and R.A. Scholtz. Impulse radio: how it works. *Communications Letters, IEEE*, 2(2):36–38, Feb 1998.
- [6] J.M. Cramer, R.A. Scholtz, and M.Z. Win. Spatio-temporal diversity in ultra-wideband radio. In *Wireless Communications and Networking Conference, 1999. WCNC. 1999 IEEE*, pages 888–892 vol.2, 1999.
- [7] IEEE Std 802.15.4-2011: Part 15.4: Low-Rate Wireless Personal Area Networks (LR-WPANs). <http://standards.ieee.org/getieee802/download/802.15.4-2011.pdf>.
- [8] M.R. Mahfouz, A.E. Fathy, M.J. Kuhn, and Y. Wang. Recent trends and advances in UWB positioning. In *Wireless Sensing, Local Positioning, and RFID, 2009. IMWS 2009. IEEE MTT-S International Microwave Workshop on*, pages 1–4, Sep 2009.
- [9] L. Zwirello, T. Schipper, M. Harter, and T. Zwick. UWB localization system for indoor applications: Concept, realization and analysis. *Journal of Electrical and Computer Engineering*, 2012:11, 2012.
- [10] C. Zhang, M. Kuhn, B. Merkl, M. Mahfouz, and A.E. Fathy. Development of an UWB indoor 3D positioning radar with millimeter accuracy. In *Microwave Symposium Digest, 2006. IEEE MTT-S International*, pages 106–109, Jun 2006.
- [11] B. Silva, Z. Pang, J. Akerberg, J. Neander, and G. Hancke. Experimental study of UWB-based high precision localization for industrial applications. In *Ultra-WideBand (ICUWB), 2014 IEEE International Conference on*, pages 280–285, Sep 2014.
- [12] R. Hach. Symmetric double sided two-way ranging,”. *IEEE P802.15 Working Group for Wireless Personal Area Networks (WPAN)*, Jun 2005.
- [13] C. McElroy, D. Neiryck, and M. McLaughlin. Comparison of wireless clock synchronization algorithms for indoor location systems. In *Communications Workshops (ICC), 2014 IEEE International Conference on*, pages 157–162, Jun 2014.
- [14] DecaWave Ltd. *DW1000 User Manual - How to use, configure and program the DW1000 UWB transceiver 2.02*, 2014.
- [15] R. B. Langley. Dilution of precision. *GPS world*, May 1999.
- [16] Y. He and A. Bilgic. Iterative least squares method for global positioning system. *Advances in Radio Science*, 9:203–208, 2011.
- [17] u-blox. *M8 Receiver Description and Protocol Specification*, Dec 2014.
- [18] u-blox. *Application Note - Datum Transformations of GPS Positions*, Jul 1999.